Comput Mech (2018) 61:687–697
https://doi.org/10.1007/s00466-017-1474-4

ORIGINAL PAPER

A methodology for modeling surface effects on stiff and soft solids

Jin He[1,2] · **Harold S. Park**[2]

Received: 4 May 2017 / Accepted: 17 August 2017 / Published online: 2 September 2017

Abstract We present a computational method that can be applied to capture surface stress and surface tension-driven effects in both stiff, crystalline nanostructures, like size-dependent mechanical properties, and soft solids, like elastocapillary effects. We show that the method is equivalent to the classical Young–Laplace model. The method is based on converting surface tension and surface elasticity on a zero-thickness surface to an initial stress and corresponding elastic properties on a finite thickness shell, where the consideration of geometric nonlinearity enables capturing the out-of-plane component of the surface tension that results for curved surfaces through evaluation of the surface stress in the deformed configuration. In doing so, we are able to use commercially available finite element technology, and thus do not require consideration and implementation of the classical Young–Laplace equation. Several examples are presented to demonstrate the capability of the methodology for modeling surface stress in both soft solids and crystalline nanostructures.

Keywords Surface tension · Finite element · Soft tissue · Bending · Buckling

Electronic supplementary material The online version of this article (https://doi.org/10.1007/s00466-017-1474-4) contains supplementary material, which is available to authorized users.

✉ Jin He
jinhe@njtech.edu.cn

Harold S. Park
parkhs@bu.edu

1 School of Mechanical and Power Engineering, Nanjing Tech University, Nanjing 211816, China

2 Department of Mechanical Engineering, Boston University, Boston, MA 02215, USA

1 Introduction

The surfaces of solids exhibit different mechanical behavior as compared to their bulk. For both soft and hard (crystalline) solids, this is due to the fact that surface atoms have a different bonding environment, and specifically fewer bonding neighbors than do atoms that lie within the material bulk [1]. These surface effects, which are typically negligible for macroscopic solids, manifest themselves in different ways and at different length scales depending on whether the solid is soft or stiff.

In crystalline (stiff) solids, surface stress effects have been shown over the past two decades to lead to interesting, non-bulk mechanical properties in nanostructures, including size-dependent mechanical properties [2–5], unique multi-functionality, like phase transformations [6], shape memory and pseudoelasticity [7,8] and non-bulk plastic deformation mechanisms [9,10]. Much of the work that has been done to capture surface effects on nanomaterials either computationally [11–15] or analytically [16–20] is based on the Young–Laplace (Y–L) model for incorporating the effect of the surface tension in solids, though alternative computational methods based on decomposing the surface and bulk energies [21–26] have also been proposed. Named after Thomas Young and Pierre Simon Laplace, the Y–L equation was originally developed in the early nineteenth century [27,28], and describes the pressure difference across a curved interface between two fluids due to the surface tension. The Y–L equation has also been demonstrated to be effective in modeling surface effects on not only fluids, but also crystalline solids [29–31].

Similarly, there has been significant recent interest in so-called elastocapillary mechanics, where surface tension due to fluid-structure interactions has been used to change the mechanical behavior and properties of soft solids, like gels [32,33]. While the best-known example of surface tension in fluid mechanics is likely that of deforming liquid droplets, there has been interest in using it to deform solid structures and the relevant reviews are in Refs. [34,35]. This interest in using elastocapillary forces to deform soft structures has emerged since for these systems the elastocapillary number, which is defined as $\tau^0/(\mu l)$, where τ^0 is the surface tension, μ is the shear modulus and l is a characteristic length, is close to unity, implying that elastocapillary effects can be substantial for these soft materials. For example, recent work has highlighted the important role surface tension plays in the contact mechanics and adhesion of soft solids [36–38], identifying its effect on wetting, large deformations, and phase separation [39], using liquid inclusions to stiffen soft solids [40], and inducing Rayleigh-Plateau elastocapillary instabilities in soft solids [41].

Finite element (FE) models of surface tension in the context of soft solids have also emerged within the past decade. Examples include the works of Saksono and Peric [42], Javili et al. [25], Henann and Bertoldi [43], Seifi and Park [44,45], and Wang and Henann [46]. As in the case of crystalline solids, all of these works have captured surface tension effects using the Y–L model. Recently, a method without using the Y–L model based on the commercial FE software ANSYS [47] was proposed [48], in which the surface tension is taken into account by utilizing a special feature of the structural surface element type SURF153 or SURF154 provided by ANSYS, where the surface tension induced in-plane force is applied to the surface nodes by assuming the surface nodes are coplanar. However, this surface element does not account for surface curvature [47], and furthermore, such surface elements are generally not used in other commercial FE codes.

Our objective in the present work is to present a FE model that captures surface effects, and can be applied to either stiff or soft solids that undergo arbitrary deformations, including bending and surface curvature, using commercially used FE codes. One motivation for this work is the realization that the out-of-plane force induced from the in-plane surface stress on a curved interface of a solid, described by the Y–L equation, can alternatively be captured using geometric nonlinearity. In doing so, we arrive at a formulation that can exploit conventional FE methods. We additionally demonstrate in 2D that the expression of the out-of-plane force induced from the in-plane surface stress without using the Y–L equation is identical to that obtained using the Y–L equation. Any FE code with shell and solid type elements, as well as the features of initial stress and geometric nonlinearity, can be used to capture surface effects on stiff and soft solids, which are demonstrated by using the commercially-available FE codes ANSYS [47] and COMSOL [49]. Without explicitly using the Y–L equation, the methodology implicitly mimics the out-of-plane force induced from the in-plane surface stress through formulating the surface stress induced force with respect to the deformed configuration of the shell through geometric nonlinear analysis.

We present a range of numerical examples demonstrating the ability of the method to capture surface effects on both stiff and soft solids. We additionally demonstrate that time-dependent material behavior, through viscoelasticity, and strain-dependent surface stresses, which are critical for stiff nanomaterials, and have recently become of interest in the mechanics of soft solids [33], can be easily accounted for through the standard options in ANSYS and COMSOL. Overall, directly incorporating surface tension-related effects into a commercial FE code should enhance the ability of scientists and engineers to model, design, study, and understand mechanical problems involving surface effects. All input files with detailed modeling procedures, geometric and mesh sizes, as well as material properties are provided in the electronic supplemental material.

2 Method overview

In this section, we first present an overview of our proposed methodology. After doing so, we also present a comparison between the proposed approach and the Y–L equation, to establish that the proposed approach reproduces the Y–L equation.

To consider the effects of surface stress, we show in Fig. 1a a solid with a surface, in which the surface stress acts on the zero-thickness film enveloping the core. This kinematic model (solid with a zero thickness surface) has been used previously in both the Y–L model as well as the well-known Gurtin-Murdoch theory of surface elasticities [30,50]. However, the notion of a zero thickness surface presents some challenges for formulating a core-shell surface stress model, as shown in Fig. 1b, and therefore our method is based on converting surface tension and surface elasticity on a zero-thickness surface to an initial stress and the corresponding elastic properties on an equivalent finite thickness shell.

The constitutive equation for the surface stress tensor τ_{ij} in Fig. 1a for the zero-thickness surface, in the first order approximation, can be written as [51,52]

$$\tau_{ij} = \tau_{ij}^0 \delta_{ij} + S_{ijkl}\epsilon_{kl} \quad (i, j, k, l = 1, 2), \tag{1}$$

where indicial notation is used, τ_{ij}^0 is the surface tension, δ_{ij} is the Kronecker delta, S_{ijkl} is the surface elasticity, and ϵ_{kl} is the Green strain. The Green strain is written as

$$\boldsymbol{\epsilon} = \frac{1}{2}(\boldsymbol{F}^{\boldsymbol{T}}\boldsymbol{F} - \boldsymbol{I}), \tag{2}$$

where $\boldsymbol{F}$ is deformation gradient and $\boldsymbol{I}$ is the identity matrix. The Green strain is introduced here since the following computations are based on finite deformation theory.

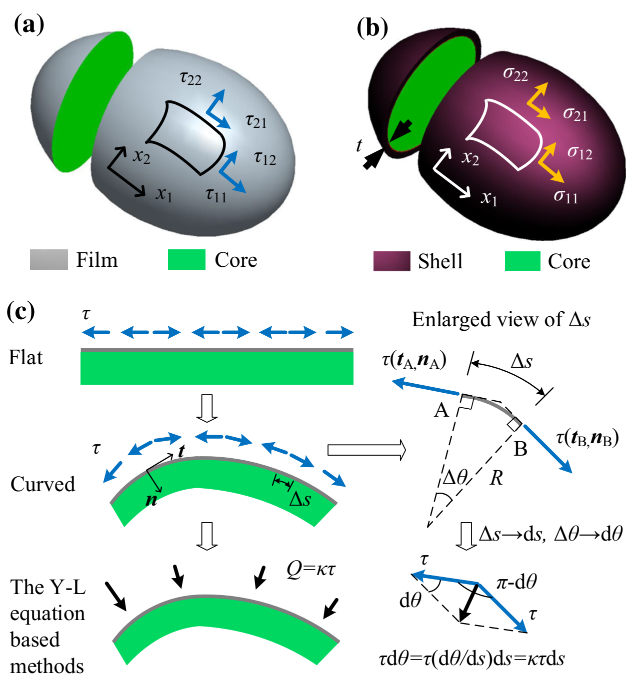

Fig. 1 The solid with the surface. **a** Core-film model; **b** Core-shell model; **c** Difference between the Y–L equation-based methods and the present methodology

On the right hand side of Eq. 1, the first term corresponds to the strain-independent part of the surface stress and the second term corresponds to the strain-dependent part of the surface stress, which represents the first order approximation of the Shuttleworth effect.

When S_{ijkl} is orthotropic and $S_{ijkl} = S_{klij}$, Eq. 1 is analogous to Eq. 3 below, which is written in the current coordinate system and describes the stress-strain relationship of an orthotropic, finite thickness shell in Fig. 1b under plane stress with initial stress σ_{ij}^0

$$\begin{bmatrix} \sigma_{11} \\ \sigma_{22} \\ \sigma_{12} \end{bmatrix} = \begin{bmatrix} \sigma_{11}^0 \\ \sigma_{22}^0 \\ 0 \end{bmatrix} + \frac{1}{1-\nu_{12}\nu_{21}} \begin{bmatrix} E_1 & E_2\nu_{12} & 0 \\ E_1\nu_{21} & E_2 & 0 \\ 0 & 0 & (1-\nu_{12}\nu_{21})G_{12} \end{bmatrix} \begin{bmatrix} \epsilon_{11} \\ \epsilon_{22} \\ \epsilon_{12} \end{bmatrix}, \tag{3}$$

where E_1, E_2 are the Young's moduli in the x_1, x_2 directions respectively, ν_{12}, ν_{21} are the major, minor Poisson's ratio in the x_1x_2 plane respectively, G_{12} is the shear modulus in the x_1x_2 plane, and σ_{ij} $(i, j = 1, 2)$ is the second Piola-Kirchhoff stress, which is work conjugate to the Green strain. The relationship between the surface stress and the strain in Eq. 1 is alternatively expressed by dividing by the shell thickness t, which leads to

$$\begin{cases} \sigma_{ij}^0 = \tau_{ij}^0\delta_{ij}/t \quad (i, j = 1, 2) & \text{(4a)} \\ E_1 = (S_{1111}S_{2222} - S_{1122}^2)/(S_{2222}t) & \text{(4b)} \\ E_2 = (S_{1111}S_{2222} - S_{1122}^2)/(S_{1111}t) & \text{(4c)} \\ G_{12} = S_{1212}/t & \text{(4d)} \\ \nu_{12} = S_{1122}/S_{2222} & \text{(4e)} \\ \nu_{21} = S_{1122}/S_{1111}. & \text{(4f)} \end{cases}$$

Since plane stress is assumed, t needs to be far less than the smallest dimension of the solid. When the surface is isotropic, $\tau_{11}^0 = \tau_{22}^0 = \tau^0$ and Eq. 1 is simplified as

$$\tau_{ij} = \tau^0\delta_{ij} + \lambda_s\epsilon_{kk} + 2\mu_s\epsilon_{ij} \quad (i, j, k = 1, 2), \tag{5}$$

where λ_s and μ_s are referred as surface Lamé constants [50], which can be obtained by imposing the symmetries of the isotropic surface [52,53]

$$\begin{cases} \lambda_s = S_{1122} & \text{(6a)} \\ \mu_s = (S_{1111} - S_{1122})/2. & \text{(6b)} \end{cases}$$

Substituting Eq. 6 into Eq. 4 leads to the Young's modulus E and Poisson's ratio ν of the equivalent isotropic shell expressed with the surface Lamé constants [48]

$$\begin{cases} E = E_s/t & \text{(7a)} \\ \nu = \lambda_s/(\lambda_s + 2\mu_s), & \text{(7b)} \end{cases}$$

where the surface Young's modulus E_s is

$$E_s = 4\mu_s(\lambda_s + \mu_s)/(\lambda_s + 2\mu_s). \tag{8}$$

The core of the solid conforms to the laws of classical solid mechanics and can be modeled as appropriate for the material system under consideration, i.e. linear elastic, hyperelastic, viscoelastic, etc. The whole shell-core structure is analyzed as a conventional solid, which can be subject to arbitrary loads and deformations, including bending.

The methodology described above is sufficiently simple that it can be implemented in any commercially-available FE package that contains both solid (for the bulk) and shell elements (for the surface). We use both ANSYS [47] and COMSOL [49] in the present work to demonstrate the versatility and ease of implementation of the proposed method.

2.1 Comparison with Y–L equation

We now present an analysis of the proposed approach, and demonstrate its equivalence with the Y–L model. The Y–L model has the feature that when the surface is flat, the surface tension results in an in-plane component only. However, when the surface is curved, the surface tension has components both in and out of the plane of the surface. According to the Y–L equation, the surface stress induced out-of-plane force per area Q_{ij} for curved surfaces is [31,51]

$$Q_{ij}n_i n_j = \kappa_{ij}\tau_{ij} \quad (i, j = 1, 2), \tag{9}$$

where n_i is the normal to the surface and κ_{ij} is the curvature tensor. When Eq. 1 is formulated in the coordinate system for the deformed configuration, the out-of-plane force component described by the Y–L equation is implicitly realized by formulating the surfaces stresses in the deformed configuration. Explanations are presented in a 2D schematic illustration (Fig. 1c), where the surface of a solid domain is initially flat and then curved by an external force. In 2D, Eq. 1 becomes

$$\tau = \tau^0 + S\epsilon, \tag{10}$$

where S is surface elasticity and τ, τ^0, ϵ are the surface stress, the surface tension, the strain in $\boldsymbol{t}$ direction lying in the surface respectively. $\boldsymbol{t}$ and $\boldsymbol{n}$ are the directions tangential and normal to the surface respectively. In 2D, Eq. 9 becomes

$$Q = \kappa\tau, \tag{11}$$

where Q is the out-of-plane force per area in $\boldsymbol{n}$ direction and κ is curvature as shown in the bottom left of Fig. 1c.

Consider a small segment of the curved surface Δs shown in the middle left of Fig. 1c and the enlarged view of the segment on the right side of Fig. 1c. The segment is subject to surface stress $\tau(\boldsymbol{t}_A, \boldsymbol{n}_A)$ and $\tau(\boldsymbol{t}_B, \boldsymbol{n}_B)$ at points A and B respectively. Since the segment is small, the segment can be approximated as an arc of a circle with radius R. The central angle of the arc is $\Delta\theta = \Delta s/R$ and the curvature of the arc is $\kappa = 1/R = \Delta\theta/\Delta s$. As the segment becomes infinitely small, $\Delta s \to \mathrm{d}s$, $\Delta\theta \to \theta$, point A approaches point B, and the strain at A has the same magnitude as the strain at B, leading to the same magnitude of the two surface stresses τ at one point. The angle of the two surface stresses is $\pi - \mathrm{d}\theta$. The net force on the the segment ds is $\tau \mathrm{d}\theta = \tau(\mathrm{d}\theta/\mathrm{d}s)\mathrm{d}s = \kappa\tau\mathrm{d}s$, in direction of $\boldsymbol{n}$. The net force divided by ds is the out-of-plane force per area $\kappa\tau$, identical to the 2D Y–L equation shown in Eq. 11. This net force is captured in the present work through geometric nonlinearity, which ensures that the surface stress calculations are performed in the deformed configuration.

3 Numerical examples

We now present numerical examples demonstrating the performance of the proposed approach for problems relevant to soft solids, involving elastocapillary phenomena, as well as surface stress effects on the mechanical properties of crystalline nanostructures. As previously mentioned, we use both ANSYS [47] and COMSOL [49] to demonstrate the ease of use and implementation in widely used commercial FE packages. The input files with detailed modeling procedures, geometric and mesh sizes, as well as material properties are provided in the Online Supplementary Materials.

3.1 Rayleigh-plateau instability

One of the most interesting findings with regards to elastocapillary effects on the deformation of soft solids was the recent experimental report of surface-tension-induced Rayleigh-Plateau instability in soft gels [41]. In this experiment, researchers increased the elastocapillary number on a soft gel until the gel broke up in a manner similar to the classical Rayleigh-Plateau instability in fluids. Subsequent researchers have investigated this effect further [54–58].

We simulated this problem using ANSYS, by considering a soft, incompressible rod with shear modulus $\mu = 12$ Pa and radius $R = 150\,\mu$m. Both ends of the rod are clamped and the rod has an aspect ratio of 200 in the ANSYS model, where 8-node element SOLID185 and 4-node element SHELL181 are used for modeling the core and the shell respectively. The material model of the core is modeled as Neo-Hookean and the shell is linear elastic. The initial shell-curvature effect is considered by setting KEYOPT(5) of the SHELL181 element to 1 in order to improve the accuracy in modeling the strain in the cross-sectional direction. The numbers of elements along the length and cross-sectional directions are 1000 and 28 respectively. Surface stress resides in a few atomic layers of a crystal according to molecular dynamic simulations [59]. In the following computations, the shell thickness t is arbitrarily chosen to be 0.1 nm. Choosing different values of t does not lead to discernible results as long as t is far less than the critical dimension of the material. The critical dimension of this problem is 150 µm.

We show in Fig. 2a the sinusoidal variation of the displacement field along the axial direction, which is characteristic of the elastocapillary Rayleigh-Plateau instability [58] of the rod, if the surface tension is 11 mN/m. In contrast, if the surface tension is slightly smaller, i.e. 10 mN/m as in Fig. 2a, no Rayleigh-Plateau instability occurs. Figs. 2a and b present about half of the rod including the contours of the displacement magnitude, where the deformations are magnified 10^5 times for better illustration. In accordance with previous analytic studies of the experiments of Mora et al. [55–58], the Shuttleworth effect is neglected in ANSYS, which is ensured by making the shell Young's modulus a very small value.

The wavelength associated with the instability is plotted as a function of the surface tension in Fig. 2c, where the curve obtained from ANSYS agrees well with the curves from previous analytic studies [41,58]. The wavelengths

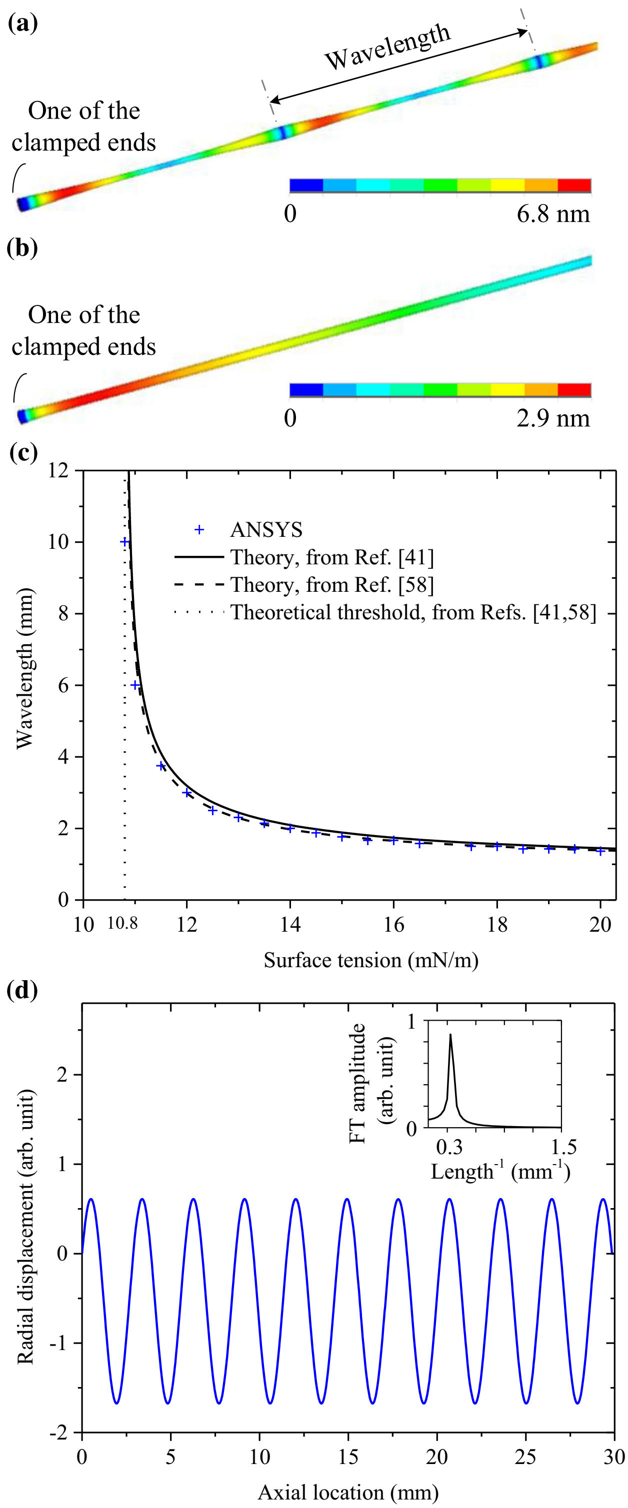

Fig. 2 Rayleigh-Plateau instabilities in soft rods. **a** The instability occurs when the surface tension is 11 mN/m. **b** The instability does not occur when the surface tension is 10 mN/m. **c** Wavelength due to the instability versus surface tension; **d** The radial displacement along the surface and the *inset* shows the corresponding FT when the surface tension is 12 mN/m

from ANSYS are obtained by performing Fourier transform (FT) of the radial displacements along the surface. As an example, the method for determining the wavelength with the surface tension of 12 mN/m is shown in Fig. 2d. The amplitude of the FT of the radial displacement reaches a peak when the inverse of the length is about 0.33 mm^{-1}, as shown in the inset of Fig. 2d, and thus the wavelength is determined to be $1/0.33 \approx 3$ mm. The surface tension threshold calculated from ANSYS is between 10.6 and 10.8 mN/m, which matches the theoretical threshold $6\mu R = 10.8$ mN/m quite closely [41,58].

3.2 Stiffening soft solids with liquid inclusions

Another interesting elastocapillary effect that has recently been reported is that a soft solid embedded with liquid inclusions may be stiffer than its counterpart without the inclusions due to the resulting surface tension that acts on the solid [40,46]. The 3D model of a droplet in a large solid domain under far-field strains is shown in Fig. 3a, where 1/8 of the entire domain is studied due to symmetry. The major and minor diameters of the deformed droplet in Fig. 3b are l and w respectively, and the liquid is assumed to be incompressible. The Young's modulus of the incompressible soft solid is 1.7 kPa and the surface tension is $\tau^0 = 3.6$ mN/m [40]. The 3D Solid Mechanics interface and Shell interface are used to model the core and the shell respectively in COMSOL since the incompressible fluid can be implemented more easily in COMSOL than in ANSYS. In modeling the large domain, the ratio of the edge size of the cube to the radius of the sphere is chosen to be 10. Approximately 1.2×10^5 quadratic tetrahedral elements are generated in the simulation. Default settings are used for the 3D Solid Mechanics interface and Shell interface.

The aspect ratios l/w under the far-field strains $\epsilon_{11} = 5.6\%$ and $\epsilon_{22} = -1.5\%$ calculated from COMSOL are compared with the experimental and theoretical results [40] in Fig. 3c, where we initially neglect the Shuttleworth effect in COMSOL. The present results are consistent with the experiment and the theory. Both the results from COMSOL and the theory predict that the aspect ratios of the liquid inclusion become smaller when the surface tension is considered, which means that the solid is stiffened by the surface tension. We also verify that if the surface tension $\tau^0 = 0$, the COMSOL results match the analytic theory.

The scattered experimental data in Fig. 3c are due to the experimental complexities involving coating silicone gel embedded with liquid drops on a stretchable sheet and attaching fluorescent nanoparticles for displacement field measurements [40]. In Ref. [40], the experiment is performed under different combinations of ϵ_{11} and ϵ_{22}, which shows that

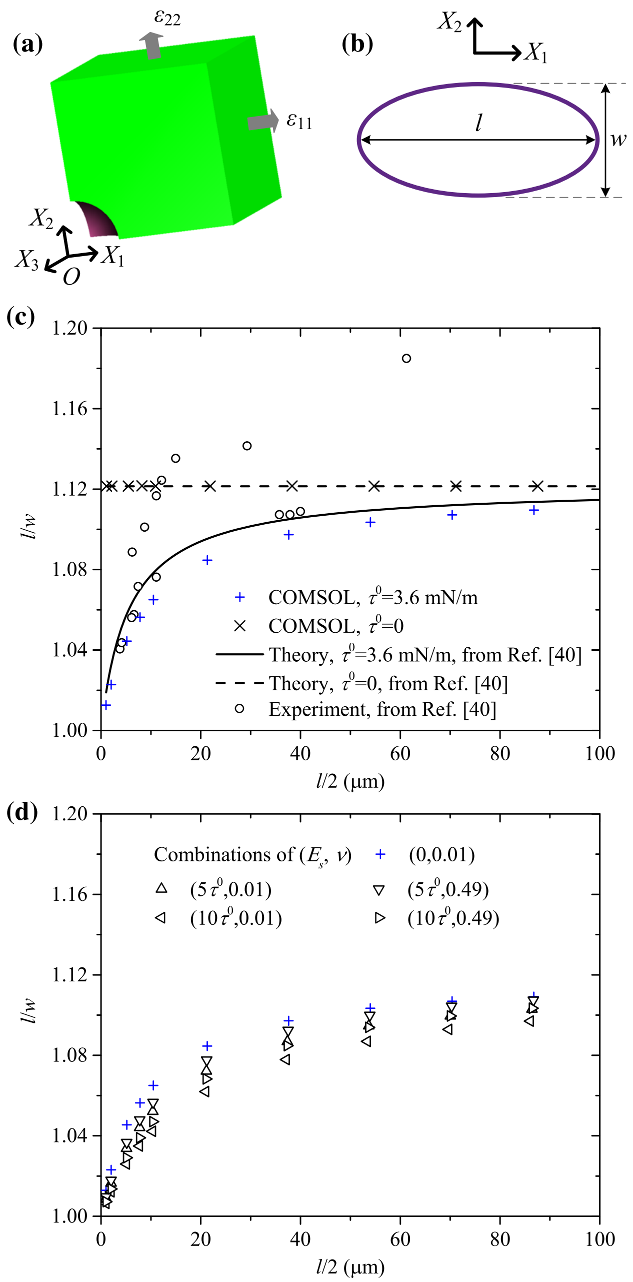

Fig. 3 The soft solid stiffened by a liquid inclusion. **a** 1/8 of the 3D model; **b** Deformed configuration in X_1X_2 plane; **c** Size-dependent aspect ratio due to the surface tension; **d** The shuttleworth effect

the curves of the size-dependent aspect ratios agree reasonably with the theory. The maximum relative difference of the aspect ratios in Fig. 3c between the COMSOL and the theory is less than 0.9%. Further mesh refinement of the COMSOL model yields to less than 0.2% difference in the aspect ratio. One of the possible causes of the slight difference between COMSOL and the theory is that small strain is assumed in the theory [60] while nonlinear kinematics are considered in the COMSOL model.

The Shuttleworth effect, whereby the surface stress is strain-dependent, has been used widely in the mechanics of crystalline nanostructures, but its effect on the mechanics of soft solids subject to surface tension has rarely been considered [33]. Here, we consider the influence of the Shuttleworth effect by assuming different combinations of surface Young's modulus and surface Poisson's ratio (E_s, ν), with the COMSOL results shown in Fig. 3d. The combination (0,0.01) corresponds to the case without the Shuttleworth effect, which is also shown in Fig. 3c. The Shuttleworth effect increases the stiffening effect of the soft solid for all the combinations: ($5\tau^0$,0.01), ($5\tau^0$,0.49), ($10\tau^0$,0.01), ($10\tau^0$,0.49), though the change in inclusion aspect ratios due to the Shuttleworth effect appears to be smaller than 5%.

3.3 Surface tension effects on relaxation of a viscoelastic half-space subject to a point force

Most of the studies related to elastocapillary effects on soft solids have not considered the time-dependent deformation of the solid, or viscoelastic effects [33]. Viscoelasticity can have a significant effect as most soft solids exhibit varying degrees of rate-dependent material behavior. Furthermore, consideration of such effects is a useful demonstration of the different types of material behavior that can be easily considered by implementing the surface tension model into a commercial FE package.

Therefore, we consider a computational model following the theoretical solution obtained by Hui and Jagota for the effect of the surface tension on the relaxation of an incompressible viscoelastic half-space excited by a point force [61]. We model the problem using a two-dimensional axisymmetric (2DA) approach, as illustrated in Fig. 4a, b.

The short and long time shear modulus of the half-space are $\mu_0 = 50$ Pa and $\mu_\infty = 200$ Pa respectively. The relaxation time is $t_r = 1$ ms and the surface tension is $\tau^0 = 1$ mN/m. The elastocapillary lengths are $\tau^0/\mu_0 = 20\,\mu$m and $\tau^0/\mu_\infty = 5\,\mu$m. A point force $F = 1$ nN in the z direction is initially applied at location $r = 0$ for a sufficient time until the half-space is fully relaxed (Fig. 4a). After the force is suddenly removed, the z-directional displacements along the surface gradually relax to zero (Fig. 4b). The 2DA Solid Mechanics interface and Membrane interface are used to model the core and the shell respectively in COMSOL. Default settings are used for the 2DA Solid Mechanics interface and Membrane interface. In modeling the half-space, the radius of the semicircle is chosen to be $100\tau^0/\mu_0$, which is 100 times the elastocapillary length. Approximately 1.2×10^5 triangular elements are generated in the simulation. The analysis is performed in two steps – a stationary analysis with the the point force applied followed by a time dependent analysis with the point force removed.

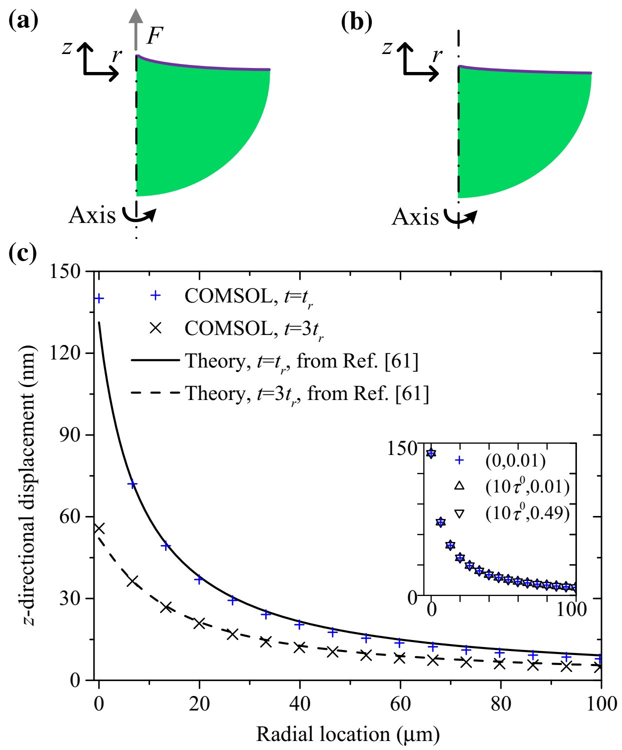

Fig. 4 The relaxation of the viscoelastic half-space excited by the point force. **a** The 2DA model with the point force applied; **b** The 2DA model with the point force removed; **c** z-directional displacements along the surface at $t = t_r$ and $3t_r$. The *inset* shows the shuttleworth effect at $t = t_r$

The z-direction displacements at $z = 0$ calculated from COMSOL agree with the theory [61] at time $t = t_r$ and $3t_r$ in Fig. 4c, where the Shuttleworth effect is neglected. The Shuttleworth effect calculated from COMSOL is presented in the inset of Fig. 4c, in which the z-directional displacements at $t = t_r$ with (E_s, ν) equal to $(10\tau^0$,0.01) and $(10\tau^0$,0.49) are almost the same as those without the Shuttleworth effect.

3.4 Surface stress effects on crystalline nanowires in bending

We now focus on validating the proposed approach in capturing the effects of surface stress on the mechanical behavior of stiff crystalline nanostructures, or nanowires (NWs). For NWs, it has been well-established that surface stress effects may influence the bending behavior of static NWs, which has been shown experimentally, theoretically, and computationally [2–4,17,62,63].

The bending NWs in clamped-free (CF) and clamped-clamped (CC) boundary conditions are in Fig. 5a, b respectively, which are modeled by using ANSYS and COMSOL in 3D. The cross section of the NWs is circular and the diameter is $D = 10$ nm. The ratio of length to diameter is 20. The element types are the same as those in the previous 3D

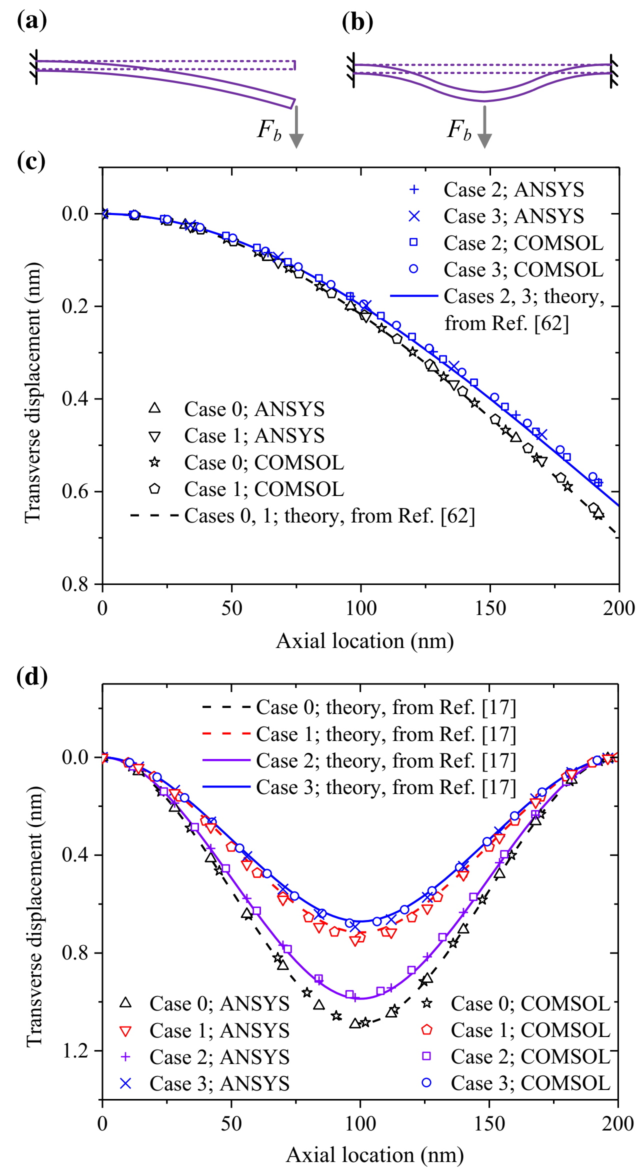

Fig. 5 The surface effects on static bending NWs. **a** CF boundary conditions; **b** CC boundary conditions; **c** Transverse displacements of the CF NW; **d** Transverse displacements of the CC NW. Case 0: no surface effects; Case 1: effect of the surface tension only; Case 2: effect of the surface elasticities only; Case 3: both effects

examples. The number of elements in length direction is 100 both in ANSYS and COMSOL. The numbers of elements in diameter direction are 16 and 8 in ANSYS and COMSOL respectively. The absolute values of the surface tension and the surface Young's modulus of face-center cubic crystal surfaces are on the order of 10^{-1} to 10^1 N/m [52]. In Fig. 5, $\tau^0 = 1$ N/m and $E_s = 10$ N/m are used for illustration purposes. The Young's modulus and the Poisson's ratio of the NW core, same as the bulk material properties, are assumed to be $E_m = 78$ GPa and $\nu_m = 0.42$ respectively. The surface tension only (Case 1), the surface elasticities only (Case 2), both effects (Case 3), and neither effects (Case 0) are studied.

Under a point transverse force $F_b = 0.01\,\text{nN}$ applied at the free end, the transverse displacements of the CF NW along the NW axial direction are shown in Fig. 5c, where the displacement curves are categorized into two groups. The transverse displacements calculated from ANSYS and COMSOL coincide with the theory [62] if the effective flexural rigidity of the circular NW is formulated as $(EI)^* = \pi E_m D^4/64 + \pi E_s D^3/8$ [17].

The surface tension does not have a significant influence on the bending behavior of the CF NW and the detailed explanations are in Ref. [62]. The CF NW appears stiffer under the influence of the surface elasticities since the surface surface Young's modulus is positive. Under $F_b = 1\,\text{nN}$ applied at the midspan of the CC NW, the transverse displacements of the CC NW are in Fig. 5d. Good agreements are found between the results from ANSYS, COMSOL, and the theory [17], where both the surface tension and the surface elasticities increase the stiffness of the CC NW.

3.5 Surface stress effects on crystalline nanowires in buckling

Our final example examines surface stress effects on the buckling of crystalline nanowires. Before presenting the results calculated by using the proposed methodology, we show theoretical derivations of the critical loads of axially buckling NWs under the influence of the surface effects based on a simplified 2D model. A CF NW, with height, depth, and length denoted as h, d, and L respectively, shown in Fig. 6a, is under an external compressive force F_a. The dimensions satisfy $L \gg d \gg h$ so that the bending in xy plane can be considered as a 2D plane strain problem as shown in Fig. 6b. In equilibrium, the total axial compressive load on the NW is the summation of the external force F_a and the counteracting force balancing the in-plane surface stress induced force $2\tau d$. Denote the transverse displacement as v. When the NW is under small bending, the out-of-plane force component, derived from the Y–L equation, is $2\tau d(\mathrm{d}^2v/\mathrm{d}x^2)$ [16–18], which can be treated as a distributed transverse force per length. Thus, the differential equation of the axis of the bending NW under the total axial compressive load $F_a + 2\tau d$ and the distributed transverse force per length $2\tau d(\mathrm{d}^2v/\mathrm{d}x^2)$ is [64]

$$(EI)^*\frac{\mathrm{d}^4v}{\mathrm{d}x^4} + (F_a + 2\tau d)\frac{\mathrm{d}^2v}{\mathrm{d}x^2} = 2\tau d\frac{\mathrm{d}^2v}{\mathrm{d}x^2}, \quad (12)$$

where the effective flexural rigidity $(EI)^*$ of the rectangular NW is [16–18]

$$(EI)^* = E_m dh^3/12 + E_s dh^2/2 + E_s h^3/6. \quad (13)$$

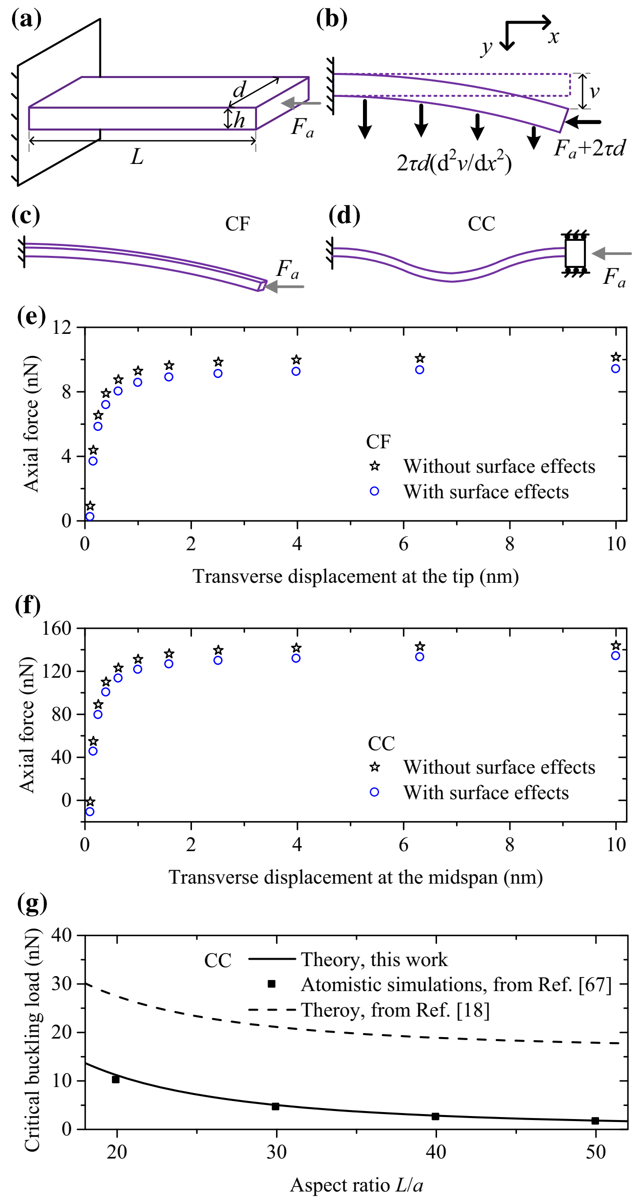

Fig. 6 The surface effects on buckling NWs. **a** CF NW satisfying $L \gg d \gg h$; **b** 2D plane strain model; **c** CF NW with square cross section; **d** CC NW with square cross section; **e** Axial force versus transverse displacement at the tip of the CF NW with $a = 10\,\text{nm}$ and $L/a = 10$; **f** Axial force versus transverse displacement at the midspan of the CC NW with $a = 10\,\text{nm}$ and $L/a = 10$; **g** Critical buckling loads of the CC NW with $a = 5.71\,\text{nm}$

Eq. 12 can be simplified as

$$(EI)^*\frac{\mathrm{d}^4v}{\mathrm{d}x^4} + F_a\frac{\mathrm{d}^2v}{\mathrm{d}x^2} = 0. \quad (14)$$

As can be seen from Eq. 14, the surface tension does not influence the critical load of the buckling CF NW if the shortening of the NW due to the surface tension is neglected. The reason is that the contribution from the out-of-plane force component due to the surface tension is completely compensated by the contribution from the in-plane axial force due to the same surface tension. We tentatively infer that Eq. 14 is suitable for buckling CF NWs with any cross-sectional geometry whenever the effective flexural rigidity is formulated accordingly, such as the buckling CF NW with a square cross section in Fig. 6c. In order to make the NW buckle, at least one end of the NW can move axially regardless of the boundary conditions, and therefore the counteracting force balancing the in-plane surface stress induced force always exists, which implies that Eq. 14 is valid for all the boundary conditions, such as the CC NW in Fig. 6d. The critical load of the axially buckling NW F_{cr}^{EB}, based on the Euler-Bernoulli beam theory, is the solution of Eq. 14

$$F_{cr}^{EB} = \pi^2 (EI)^* / (KL)^2, \tag{15}$$

where $K = 2.0$ for the CF NW and $K = 0.5$ for the CC NW [64]. The transverse shear deformation is neglected in Eq. 15, which is nontrivial for stubby NWs. Based on previous discussions and the Timoshenko beam theory [64], the critical load of the axially buckling NW F_{cr}^{T} is similar to the classical one except that the flexural rigidity is substituted by the effective flexural rigidity

$$F_{cr}^{T} = \frac{\pi^2 (EI)^* / (KL)^2}{1 + \pi^2 (EI)^* / [\beta \mu_m A (KL)^2]}, \tag{16}$$

where the shear coefficient is $\beta = 5(1+\nu_m)/(6+5\nu_m)$ for rectangular cross sections [65], μ_m is shear modulus, and A is cross-sectional area.

The calculations in studying the surface effects on the NWs in Buckling are based on gold in [001] growth direction with (001) crystal face. For the (001) crystal face of gold, the surface tension is $\tau^0 = 1.41$ N/m and the surface Young's modulus is $E_s = (S_{1111}S_{2222} - S_{1122}^2)/S_{2222} = -4.96$ N/m [52]. The Young's modulus and Poisson's ratio of macroscopic single-crystal gold in [001] direction are $E_m = 49.5$ Gpa and $\nu_m = 0.455$ respectively [66]. The CF NW (Fig. 6c) and the CC NW (Fig. 6d) have a square cross section with a side dimension of a. The curves of the axial force F_a versus the transverse displacement v of the CF and CC NWs calculated from COMSOL are in Fig. 6e and f respectively, where a is 10 nm and the aspect ratio L/a is 10. In the COMSOL model, small forces in x direction contributing to approximately $v = a/100$ are applied at the tip and the midspan of the CF and CC NWs respectively for introducing the perturbation. Increasing F_a until F_a changes slowly with respect to v leads to the critical buckling loads, which agree well with the theoretical values calculated from Eq. 16 in Table 1. The theoretical values are further compared to the results from atomistic simulations for [001]/(001) gold [67] in Fig. 6g, where the boundary conditions are CC and $a = 5.71$ nm. Good agreement is found between the theory and the atomistic simulations. For comparison, the incorrect critical buckling loads obtained from Ref. [18] are also shown in Fig. 6g, which occurs if the Y–L equation is directly applied for buckling without accounting for the axial force resulting from the surface tension.

Table 1 The critical buckling loads of the CF and CC NWs

	Without surface effects			With surface effects		
	COMSOL (nN)	Theory (nN)	Diff. %	COMSOL (nN)	Theory (nN)	Diff. %
CF	10.1	10.1	0.0	9.4	9.3	1.1
CC	143.9	146.9	−2.0	134.2	136.2	−1.5

The parameters are $a = 10$ nm, $L/a = 10$, $\tau^0 = 1.41$ N/m, $E_s = -4.96$ N/m, $E_m = 49.5$ Gpa, and $\nu_m = 0.455$

4 Conclusion

We have presented a methodology for modeling surface stress effects on both stiff and soft solids. In contrast to most previous approaches for modeling surface stress, the proposed methodology leverages the vast resources available in widely used commercial FE software packages like ANSYS and COMSOL. The present methodology is also different in that the Young–Laplace equation is not the starting point for capturing surface stress effects. Instead, we model the out-of-plane force component induced by the surface tension in curved surfaces through geometric nonlinear analysis. The essence of the methodology is to convert the surface tension and the surface elasticities in the zero-thickness surface to an initial stress and corresponding elastic properties in the equivalent finite-thickness shell. The results obtained by using the methodology are consistent with previous experimental and analytical work where surface tension impacts both stiff and soft solids. The methodology offers extensive opportunities for performing complex multidisciplinary modeling work such as electromechanical coupling, fluid-structural coupling, and thermomechanical coupling in the solid systems by exploiting the built-in functionality of commercial FE codes under the influence of the surface tension or surface stress.

Acknowledgements This work is supported by the National Natural Science Foundation of China (Grant No. 11504170). Both authors acknowledge the support of the Department of Mechanical Engineering at Boston University.

References

1. Cammarata RC, Sieradzki K (1994) Surface and interface stresses. Annu Rev Mater Sci 24:215

2. Park HS, Cai W, Espinosa HD, Huang H (2009) Mechanics of crystalline nanowires. MRS Bull 34(3):178
3. Cuenot S, Fretigny C, Demoustier-Champagne S, Nysten B (2004) Surface tension effect on the mechanical properties of nanomaterials measured by atomic force microscopy. Phys Rev B 69(16):165410
4. Jing GY, Duan HL, Sun XM, Zhang ZS, Xu J, Li YD, Wang JX, Yu DP (2006) Surface effects on elastic properties of silver nanowires: contact atomic-force microscopy. Phys Rev B 73(23):235409
5. Chen CQ, Shi Y, Zhang YS, Zhu J, Yan YJ (2006) Size dependence of Young's modulus in ZnO nanowires. Phys Rev Lett 96(7):075505
6. Diao J, Gall K, Dunn ML (2003) Surface-stress-induced phase transformation in metal nanowires. Nat Mater 2(10):656
7. Park HS, Gall K, Zimmerman JA (2005) Shape memory and pseudoelasticity in metal nanowires. Phys Rev Lett 95:255504
8. Liang W, Zhou M, Ke F (2005) Shape memory effect in Cu nanowires. Nano Lett 5(10):2039
9. Park HS, Gall K, Zimmerman JA (2006) Deformation of FCC nanowires by twinning and slip. J Mech Phys Solids 54(9):1862
10. Weinberger CR, Cai W (2012) Plasticity of metal nanowires. J Mater Chem 22(8):3277
11. Gao W, Yu SW, Huang GY (2006) Finite element characterization of the size-dependent mechanical behaviour in nanosystems. Nanotechnology 17(4):1118
12. He J, Lilley CM (2009) The finite element absolute nodal coordinate formulation incorporated with surface stress effect to model elastic bending nanowires in large deformation. Comput Mech 44(3):395
13. Yvonnet J, Mitrushchenkov A, Chambaud G, He QC (2011) Finite element model of ionic nanowires with size-dependent mechanical properties determined by ab initio calculations. Comput Methods Appl Mech Eng 200(5–8):614
14. Farsad M, Vernerey FJ, Park HS (2010) An extended finite element/level set method to study surface effects on the mechanical behavior and properties of nanomaterials. Int J Numer Methods Eng 84(12):1466
15. Yvonnet J, Quang HL, He QC (2008) An XFEM/level set approach to modelling surface/interface effects and to computing the size-dependent effective properties of nanocomposites. Comput Mech 42:119
16. Wang GF, Feng XQ (2007) Effects of surface elasticity and residual surface tension on the natural frequency of microbeams. Appl Phys Lett 90(23):231904
17. He J, Lilley CM (2008) Surface effect on the elastic behavior of static bending nanowires. Nano Lett 8(7):1798
18. Wang GF, Feng XQ (2009) Surface effects on buckling of nanowires under uniaxial compression. Appl Phys Lett 94:141913
19. Sharma P, Ganti S, Bhate N (2003) Effect of surfaces on the size-dependent elastic state of nano-inhomogeneities. Appl Phys Lett 82(4):535
20. He J, Lilley CM (2008) Surface stress effect on bending resonance of nanowires with different boundary conditions. Appl Phys Lett 93(26):263108
21. Park HS, Klein PA, Wagner GJ (2006) A surface Cauchy–Born model for nanoscale materials. Int J Numer Methods Eng 68:1072
22. Park HS, Klein PA (2007) Surface Cauchy–Born analysis of surface stress effects on metallic nanowires. Phys Rev B 75:085408
23. Park HS, Klein PA (2008) A surface Cauchy–Born model for silicon nanostructures. Comput Methods Appl Mech Eng 197:3249
24. Javili A, Steinmann P (2009) A finite element framework for continua with boundary energies. Part I: the two-dimensional case. Comput Methods Appl Mech Eng 198:2198
25. Javili A, Steinmann P (2010) A finite element framework for continua with boundary energies. Part II: the three-dimensional case. Comput Methods Appl Mech Eng 199:755
26. Yang Q, To AC (2017) Multiresolution molecular mechanics: surface effects in nanoscale materials. J Comput Phys 336:212
27. Young T (1805) An essay on the cohesion of fluids. Philos Trans R Soc Lond 95:65
28. Laplace PS (1805) Trait*é* de M*é*canique C*é*leste, vol 4. Gauthier-Villars, Paris
29. Shuttleworth R (1950) The surface tension of solids. Proc Phys Soc Lond Sect A 63(5):444
30. Gurtin ME, Murdoch AI (1975) A continuum theory of elastic material surfaces. Arch Ration Mech Anal 57(4):291
31. Chen TY, Chiu MS, Weng CN (2006) Size dependence of young's modulus in ZnO nanowires. J Appl Phys 100(7):5
32. Andreotti B, Baumchen O, Boulogne F, Daniels KE, Dufresne ER, Perrin H, Salez T, Snoeijer JH, Style RW (2016) Solid capillarity: when and how does surface tension deform soft solids? Soft Matter 12:2993
33. Style RW, Jagota A, Hui C-Y, Dufresne ER (2016) Elastocapillarity: surface tension and the mechanics of soft solids. Annu Rev Condens Matter Phys 8:99–118
34. Roman B, Bico J (2010) Elasto-capillarity: deforming an elastic structure with a liquid droplet. J Phys: Condens Matter 22:493101
35. Liu JL, Feng XQ (2012) On elastocapillarity: a review. Acta Mech Sin 28(4):928
36. Style RW, Dufresne ER (2012) Static wetting on deformable substrates, from liquids to soft solids. Soft Matter 8(27):7177
37. Style RW, Boltyanskiy R, Che Y, Wettlaufer J, Wilen LA, Dufresne ER (2013) Universal deformation of soft substrates near a contact line and the direct measurement of solid surface stresses. Phys Rev Lett 110(6):066103
38. Style RW, Hyland C, Boltyanskiy R, Wettlaufer JS, Dufresne ER (2013) Surface tension and contact with soft elastic solids. Nat Commun 4:2728
39. Jensen KE, Sarfati R, Style RW, Boltyanskiy R, Chakrabarti A, Chaudhury MK, Dufresne ER (2015) Wetting and phase separation in soft adhesion. Proc Nat Acad Sci 112(47):14490
40. Style RW, Boltyanskiy R, Allen B, Jensen KE, Foote HP, Wettlaufer JS, Dufresne ER (2015) Stiffening solids with liquid inclusions. Nat Phys 11(1):82
41. Mora S, Phou T, Fromental JM, Pismen LM, Pomeau Y (2010) Capillarity driven instability of a soft solid. Phys Rev Lett 105(21):214301
42. Saksono PH, Peric D (2006) On finite element modelling of surface tension. Variational formulation and applications—part I: quasistatic problems. Comput Mech 38:265
43. Henann DL, Bertoldi K (2014) Modeling of elasto-capillary phenomena. Soft Matter 10:709
44. Seifi S, Park HS (2016) Computational modeling of electro-elasto-capillary phenomena in dielectric elastomers. Int J Solids Struct 87:236
45. Seifi S, Park HS (2017) Electro-elastocapillary rayleigh-plateau instability in dielectric elastomer films. Soft Matter 13:4305
46. Wang Y, Henann DL (2016) Finite-element modeling of soft solids with liquid inclusions. Extreme Mech Lett 9:147
47. ANSYS (2016) Mechanical APDL 17.0
48. He J (2015) Surface stress on the effective Young's modulus and Poisson's ratio of isotropic nanowires under tensile load. AIP Adv 5(11):117206
49. COMSOL (2016) COMSOL multiphysics user's guide, version 5.2a
50. Gurtin ME, Murdoch AI (1978) Surface stress in solids. Int J Solids Struct 14(6):431
51. Miller RE, Shenoy VB (2000) Size-dependent elastic properties of nanosized structural elements. Nanotechnology 11(3):139
52. Shenoy VB (2005) Atomistic calculations of elastic properties of metallic fcc crystal surfaces. Phys Rev B 71(9):094104

53. Shenoy VB (2006) Erratum: Atomistic calculations of elastic properties of metallic fcc crystal surfaces [Phys. Rev. B 71, 094104 (2005)]. Phys Rev B 74(14):149901
54. Barriere B, Sekimoto K, Leibler L (1996) Peristaltic instability of cylindrical gels. J Chem Phys 22:1735
55. Cialetta P, Amar MB (2012) Peristaltic patterns for swelling and shrinking of soft cylindrical gels. Soft Matter 8:1760
56. Mora S, Phou T, Fromental JM, Pismen LM, Pomeau Y (2010) Capillarity driven instability of a soft solid. Phys Rev Lett 105:214301
57. Taffetani M, Ciarletta P (2015) Beading instability in soft cylindrical gels with capillary energy: weakly non-linear analysis and numerical simulations. J Mech Phys Solids 81:91
58. Xuan C, Biggins J (2016) Finite-wavelength surface-tension-driven instabilities in soft solids, including instability in a cylindrical channel through an elastic solid. Phys Rev E 94(2):023107
59. Muller P, Saul A (2004) Elastic effects on surface physics. Surf Sci Rep 54(5–8):157
60. Duan HL, Wang J, Huang ZP, Karihaloo BL (2005) Eshelby formalism for nano-inhomogeneities. Proc R Soc Math Phys Eng Sci 461(2062):3335
61. Hui CY, Jagota A (2016) Effect of surface tension on the relaxation of a viscoelastic half-space perturbed by a point load. J Polym Sci Part B-Polym Phys 54(2):274
62. Song F, Huang GL, Park HS, Liu XN (2011) A continuum model for the mechanical behavior of nanowires including surface and surface-induced initial stresses. Int J Solids Struct 48(14–15):2154
63. Yun G, Park HS (2009) Surface stress effects on the bending properties of fcc metal nanowires. Phys Rev B 79:195421
64. Timoshenko SP, M GJ (1961) Theory of elastic stability, 2nd edn. McGraw-Hill, NY
65. Hutchinson JR (2001) Sheer coefficients for Timoshenko beam theory. J Appl Mech-Trans ASME 68(1):87
66. Gan Y, Sun Z, Chen Z (2015) Extensional vibration and size-dependent mechanical properties of single-crystal gold nanorods. J Appl Phys 118(16):164304
67. Olsson PAT, Park HS (2012) On the importance of surface elastic contributions to the flexural rigidity of nanowires. J Mech Phys Solids 60(12):2064